

# OPTIMIZATION OF EYE-SAFE APD LIDAR FOR AUTOMOBILE SAFETY AND AUTOMATED NAVIGATION SYSTEMS

By George M. Williams, Jr  
 Allegro MicroSystems

## INTRODUCTION

Newly emergent accident-reducing driver-assistance and automated-navigation technology for automobiles is based on real-time three-dimensional (3-D) mapping and object detection, tracking, and classification using lidar sensors. Yet, the lack of lidar sensors suitable for meeting application requirements appreciably limits practical widespread use of lidar in trucking, public livery, consumer cars, and fleet automobiles. To address this need, a system-engineering perspective to eye-safe lidar-system design for high-level advanced driver-assistance sensor systems and a design trade study including 1.5-micron spot-scanned, line-scanned, and flash-lidar systems are presented. A cost-effective lidar instrument design is then proposed based on high-repetition-rate diode-pumped solid-state lasers and high-gain low-excess-noise InGaAs avalanche-photodiode receivers and sensor arrays. Using probabilistic receiver-operating-characteristic analysis derived from measured component performance, a design is presented for a compact lidar system that is capable of 220-meter ranging with 5 cm accuracy and that can be readily scaled to a 360-degree field of regard.

## BACKGROUND

The critical component to a new class of cost-effective, high-performance automobile driver-assistance sensor (ADAS) and automated-driving system is a sensor that can capture motion-distortion-free range and intensity data that are accurate, high resolution, and able to be used to create extremely detailed, high-definition 3-D maps of surroundings in real time, including those that may be georeferenced to real-world coordinates. The market previously addressed several of these objectives with radar, ultrasound,

and vision sensors. However, radar sensors, while offering a range of 200 meters or better, are expensive and lack angular resolution; ultrasound sensors lack the necessary range and resolution capabilities; and vision sensors lack the necessary long-distance range performance. Compared to these current market solutions, eye-safe lidar sensors offer improved performance for long-distance object detection and mapping in low-visibility conditions, and enable the realization of compact, cost-effective sensor systems.

The benefits of lidar stem from the principles of its operation (e.g., Figure 1).

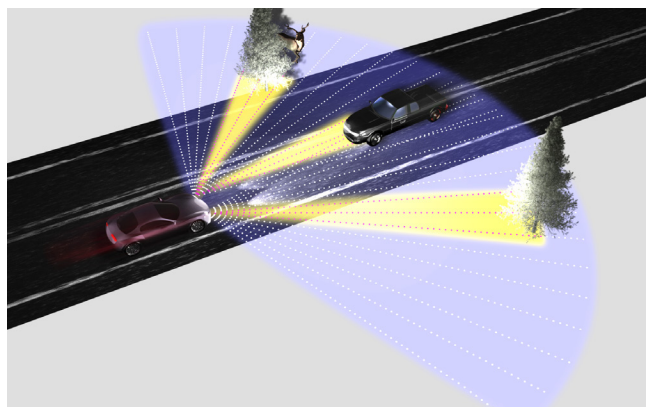


Figure 1: Lidar bounces light beams off objects rather than using radio waves, as with radar. In an automated car, it works with radar and cameras to give the vehicle 360-degree vision of its surroundings.

A lidar device emits rapid bursts of short-pulsed infrared laser light, in a very similar fashion to the sound waves of sonar sensing or the radar waves of radar sensing. Unlike radar, which employs large radio-frequency waves and captures low-resolution 3-D images at no better than

0.5-meter resolution, lidar employs optical waves ~500× shorter than radar waves, and lidar can capture higher-resolution 3-D images with finer depth precision. The light travels toward whatever object is in its path, then reflects back toward the device. Since the speed of light is well known, lidar sensors can determine the range to a target through measurement of the time it takes for the light to return to the origin. In this way, azimuth-elevation-range and range rate measurements may be captured. The use of reflected laser light also allows the reflectivity of objects to be measured—independent of ambient light—enabling lidar to provide long-distance high-fidelity range imaging for a wide range of conditions. Because lidar uses its own light source, it avoids problems associated with video cameras, which do not operate well in dark conditions and are prone to high false-alarm rates (FARs) and saturation in brightly lit conditions.

While it is inevitable that the near future will bring automated-navigation and ADAS systems that play important roles in automobile safety and navigation, despite its significant promise, the role that lidar sensors will play, among the suite of sensors, is yet to be determined. Existing automobile lidar sensors have yet to achieve the necessary range and resolution performance in inclement conditions, and significant improvements need to be made to the lidar system size, weight, and power, as well as the cost and reliability. The lack of suitable lidar instruments appreciably limits practical widespread use of lidar in a wider range of ADAS applications, and arguably has slowed the proliferation of Level 3 and higher automated driving systems.<sup>[1]</sup>

The ideal lidar sensor is a reliable low-cost all-weather camera that can capture temporally registered and calibrated, high-dimensionality angle-angle-range point-cloud data fully from around the vehicle (360 degrees) using non-mechanical scanning, with a sufficiently fast update rate to avoid vehicle-motion artifacts and to provide sub-ms response time. As opposed to the capture of a single range return, the ideal sensor might be configured to efficiently capture and provide to the system increased dynamic data—such as scene attributes encoded in a return pulse waveform, including reflectivity, pulse shape, and polarization—as a function of the average laser power expended.

Lidar applications can be grouped into two primary distance zones of interest: a medium distance of approximately 20 – 40 meters for side and angular warning zones, and

a long distance of 150 – 400 meters for the front and rear warning zones. Medium-distance lidar sensors generally require multi-location placement and, as they must fit within the body panels of the vehicle, size is a consideration. To reduce the number of sensors needed, each must have a large field of view (FOV), generally more than 100 degrees in azimuth.

A long-distance lidar has a field of regard (FOR) that includes all, or a significant part, of the 360-degree azimuth, with a field of regard in elevation that extends from the foot of a pedestrian located one meter away to vehicles 400 meters or farther down the road, resolved to better than 0.1-degree angular resolution and centimeter-scale range accuracy.

A notional long-distance lidar sensor requirement is specified in Table 1. The challenge is to determine the lidar system architecture that best meets these requirements, given the available transmitter, receiver, and optical technologies.

## SELECTING OPERATING WAVELENGTH

The cost and performance of the current lidar systems can be traced to the choice of sensor architecture, based on the chosen laser transmitter and detector technologies. While use of commercially available 905 nm diodes is often attributed to a compatibility with cost-effective silicon detector technology, the large depletion depth of near-infrared optical radiation in silicon makes photodetectors manufactured using deep-submicron CMOS processes largely inefficient or slow to respond to pulsed 905 nm light. When a single detector element or a small detector array is employed, detectors made of compound semiconductor materials, such as InGaAs, may pose minimal incremental contribution to cost, and may offer enhanced temporal response and the possibility for use of lasers that pose less ocular hazard.

Both the IEC-60825-1 standard and the ANSI Z136.1 standard include methods to calculate maximum permissible exposure (MPE). The methods vary dependent on the operation and implementation of the transmitter, which is governed by the most stringent safety level. For visible and near-infrared wavelengths, the MPE levels are quite low. Collimated laser beams of 905 nm light are especially dangerous at relatively low power because the lens focuses the light onto a tiny spot on the retina. For a 905 nm, 1 ns pulse, the MPE at the cornea of a collimated beam of laser light is ~1 μJ/cm<sup>2</sup> of energy density, and ~5 mW/cm<sup>2</sup> power density for a one-second exposure

[1] Frost & Sullivan, "LiDAR: Driving the Future of Autonomous Navigation – Analysis of LiDAR Technology for Advanced Safety," Frost & Sullivan, February 9, 2016, 31 pages

Table 1: Notional Lidar Sensor Specifications for Automated Navigation

Requirements	Specification	Units
Eye Safety	Class 1	ANSI standards
Azimuth Field of Regard	360 (6.25)	degrees (radians)
Elevation Field of Regard	20 (0.35)	degrees (radians)
Angular Resolution	0.02 (0.35)	degrees (mrad)
Azimuth Samples	18,000	elements
Elevation Resolution Elements	1,000	elements
Frame Format	$1.8 \times 10^7$	elements/frame
Frame Rate (scan rate)	20 (7200)	frames per second (degree/sec)
FOR Sample Rate	$3.6 \times 10^8$	samples per second
Maximum Range	220	meters
Minimum TOF to Range	$1.47 \times 10^{-6}$	seconds
Unambiguous Laser Pulse Rate	$6.82 \times 10^5$	Hz
Sample Rate to Laser Rate Ratio	528	sample elements/pulse
Range Resolution / Time Precision	0.05 / 333	meters/ps
Range-Resolved Elements	4400	time slices (~12 bits)
Returns Per Pulse	1(3)	minimum (desired)
Analog Pulse Digitization	8	bits
Min Unencoded Data Bit Rate – 1 Sample TOF and Amp.	$7.2 \times 10^9$	bits per second
Aperture	35	mm
Laser Pulse Energy Required for 220-Meter Sensitivity	0.2	micro-Joules (10% reflective target)
Laser Pulse Energy Required for Unambiguous Data	105.6	micro-Joules
Average Power Required	72	watts

time.<sup>[2]</sup> Ocular-hazard reduction requires either: a limitation of the transmitter pulse energy, which degrades range performance and reduces performance in inclement weather; or an expansion of the transmitter optic, which increases system size and weight.

To ensure the laser is fully eye-safe (class 1M, IEC/EN 60825), the maximum pulse energy and pulse-repetition rate must be limited, and an appropriate beam expander must be used.<sup>[3],[4]</sup> At high repetition rates (i.e., greater than 55 kHz), the emission is considered to be a continuous-wave source with a power level equal to the average power emitted by the transmitter. The safety requirements that govern these laser transmitters make it difficult to provide coverage for a large field of regard, and any expansion to the laser beam to reduce the power flux density would increase the size and weight of the system.

In contrast, short-wavelength infrared (SWIR) light—with a wavelength longer than ~1,400 nm—is absorbed by the transparent parts of the eye before it reaches the retina, which means that the MPE for these wavelengths is higher than for visible light. At ~1.5 μm, the MPE is ~1 μJ/cm<sup>2</sup>, which allows for configuration with smaller-diameter collimator optics with higher radiant-intensity output than the 905 nm counterparts. This consideration makes the 1.5 μm spectral range well-suited for scanned-linear, stepped, two-dimensional (2-D) arrays and full-format flash-lidar systems. Eye safety is maintained for the high-brightness laser beams by low-duty-cycle pulsing and by the motion of the beam as it scans the FOV, such that the limits of optical power safety are not exceeded.

Further benefits of operation in the SWIR compared to operation at 905 nm are: less scattering from rain,

[2] International Electrotechnical Commission, “International Standard IEC 60825: Safety of Laser Products,” IEC, Geneva, Switzerland Edition 1.2, [https://shop.textalk.se/shop/ws26/40626/files/full\\_size\\_-\\_for\\_start\\_page\\_banner/iec60825-1%7Bed1.2%7Den.pdf](https://shop.textalk.se/shop/ws26/40626/files/full_size_-_for_start_page_banner/iec60825-1%7Bed1.2%7Den.pdf), 2001.

[3] J. D. Spinhirne, “Micro Pulse Lidar,” IEEE Transactions on Geoscience and Remote Sensing 3(1), pp. 48-55 (1993).

[4] J. A. Reagan, “New Generation Lidars to Support Aerosol Radiation / Climate Forcing Studies,” in Proc. IEEE International Geoscience and Remote Sensing Symposium 3, pp. 2313-2315 (1995).

smoke, smog, and other atmospheric elements; and less susceptibility to clutter due to in-band solar radiation.

These benefits can make use of higher pulse energy in small-area, scanning, or large-format detector arrays.

## EYE-SAFE LIDAR SYSTEM ARCHITECTURES

There are two general classes of lidar sensors—scanning and flash. Most of today’s lidar sensors are configured as single-element [i.e., one-dimensional (distance)] measurement devices combined with a mechanical beam-deflection system (e.g., a rotating mirror or scanning mirrors) to provide spatial measurements. Scanning-lidar systems and flash-lidar systems use the same technique to determine the range to a target—that is, they measure the time of flight (TOF) of a laser pulse to the target and back to the detector. However, the illumination and detection approaches differ. A scanning lidar system either performs a raster-scan of the laser spot over a region of the target surface, or uses the relative motion of the lidar platform with respect to the object. This process continues until the  $(x,y,z)$  coordinate and intensity of the entire field of regard are measured. While scanning-lidar systems are very effective for scenes that are relatively static over time, they do not perform as well in dynamic situations that require rapid ranging and imaging of an entire scene.

Ambiguity range is an important operational parameter: This is the range to an object, where the backscattered light from a given laser pulse is detected before the emission of the next laser pulse.<sup>[5],[6]</sup> The ambiguity determines the maximum laser repetition rate—and, ultimately, the peak laser power and average laser power—and is, thus, an important system-design parameter. The unambiguous laser-repetition rate for 220-meter range returns is 682 kHz, as shown in Table 1. This rate is 528× less than the ~360 MHz required to sample the 360-degree x 20-degree field of regard with the specified resolution and update rate. Because of the limitations imposed by the speed of light, either the system must be segmented into 528 individual spot-scanning lidar cameras, each with a small field of regard; or the laser output beam must be matched to the solid angles subtended by ~528 photodetector elements. When the divergence of the laser increases, more peak power is required to maintain the specified standoff range and range resolution.

Sufficient laser-pulse energy implemented with today’s rapidly maturing sensor-array technology can produce a flash-lidar system that achieves timed illumination of an FOV

without mechanical movement. In a flash-lidar system, the laser beam is diverged so that the illuminated spot on the surface closely matches the FOV of a 2-D array of detectors. In most realizations of flash lidar, the beam divergence of the laser is optically matched to the receiver FOV so that all pixels in the array are illuminated simultaneously. Each pixel in the detector array is individually triggered by the arrival of a pulse return generated within its instantaneous FOV, which allows for measurement of both intensity and TOF of one or more returns from the laser pulse. In this way, each pixel  $(x,y)$  has its own range data  $(z_0, z_1, \dots, z_{last})$ , which results in the 3-D point cloud. The resolution in  $x$  and  $y$  depends on the camera resolution, and the range resolution in  $z$  depends on the pulse width or rise time of the laser, the response time of the photodetector elements, and the resolution of the time-conversion circuits.

A clear benefit of a flash-system is that the flash system provides a full-scene frame quicker than a scanning system. The frame rate is limited only by how fast the laser can be pulsed and how fast the pixel readout can occur. Moreover, the lower capacitance of the small pixels used in 2-D detector arrays allows for higher pixel-conversion gain and lower pixel-amplifier noise, which can improve sensitivity and range resolution. In this respect, a flash-lidar sensor array may have superior sensitivity in terms of average laser power, although the peak power required to illuminate a 2-D sensor array scales proportionally to the pixel count.

Within the available trade space for practical lidar sensor designs, there are hybrids of the scanned and flash-lidar concepts. These hybrids use either a small-sized linear or 2-D detector array with an FOV matched to the laser angular divergence. In such concepts, to create the lidar image, either: the laser output and detector array are synchronously scanned across the field of regard; or large-format 2-D detector arrays are used that are configured with bright, low-divergence, or beam-shaped fan lasers that scan across the detector array.

## LIDAR SENSOR MODEL

The notional lidar-sensor specification in Table 1 describes a 360-degree (azimuth) by 20-degree (elevation) sensor with 0.02-degree angular resolution (~7 cm footprint at 220 meters) and 5 cm range resolution.

### Sensitivity

Laser beam shape, transmit-pulse energy, and light propagation path all affect the signal-return characteristics. Atmospheric absorption and scattering attenuate the

[5] Piracha, Mohammad Umar, et al. “Range resolved lidar for long distance ranging with sub-millimeter resolution.” *Optics express* 18.7 (2010): 7184-7189.  
[6] Krichel, Nils J., Aongus McCarthy, and Gerald S. Buller. “Resolving range ambiguity in a photon counting depth imager operating at kilometer distances.” *Optics express* 18.9 (2010): 9192-9206.

laser beam as it propagates, and turbulence can cause broadening, defocusing, and deflection.

Target orientation, surface texture, and reflectivity properties also affect performance. For example, the geometric complexity of the surface and the Lambertian and specular components of the target reflectivity determine how much energy is reflected back to the receiver aperture, and the orientation of the target relative to the angle of incidence can lengthen the pulse and modulate the pulse shape.

Optical efficiency, detector optical-to-electrical conversion efficiency, and photoreceiver gain-bandwidth and sensitivity properties significantly influence system performance.

The amount of laser energy returned from multi-faceted targets can be estimated as<sup>[7]</sup>:

Equation 1:

$$P_R = \frac{4KP_s T_A \eta_t \Gamma}{\pi \phi^2 R^2} \Gamma \frac{T_A}{4\pi R^2} \frac{\pi D^2 \eta_r}{4},$$

where  $PR$  is the received signal power in watts;  $K$  is the beam-profile function;  $PS$  is the transmitted laser power in watts;  $TA$  is the atmospheric transmission;  $\eta_t$  is the transmitter optical efficiency;  $\Phi$  is the beam width in radians;  $R$  is the range (monostatic system);  $\Gamma$  is the target laser cross section in meters;  $D$  is the receiver aperture diameter; and  $\eta_r$  is the receiver optical efficiency.

Equation 1 can be used to establish a photon budget for a system-design trade study; and the received signal power can easily be converted to photons for a given laser pulse duration, knowing the energy per photon. The photons expected from 30% reflective targets are shown in Figure 2, at various ranges, calculated for several laser pulse energies. Here, a 0.5 mrad laser divergence and a 30 mm-diameter receiver with 70% optical efficiency are assumed.

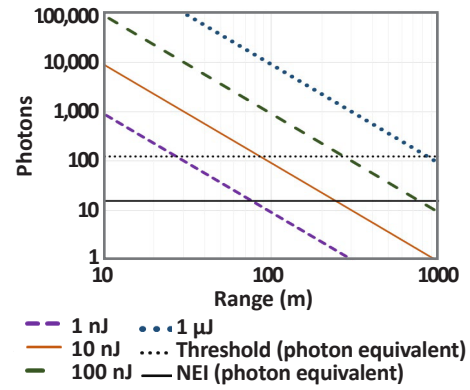


Figure 2: Modeled photon returns for the lidar receiver for 1 nJ, 10 nJ, 100 nJ, and 1 μJ pulse energies, assuming a 30 mm aperture, a 30% reflective target, and a 0.5 mrad-divergent laser.

One of the first parameters to choose when designing a lidar sensor is its threshold value (for instance, in voltage:  $V_{th}$ ) given the noise level of the photoreceiver ( $\sigma_{v,n}$ ). The threshold must be computed from the probability of false alarm (PFA) specified for a given application, i.e., the probability that a pulse of electronic noise will exceed the detection threshold in the absence of a target, resulting in a spurious detection event. The PFA and the FAR are related to each other by Poisson statistics, because the FAR is the probability density with respect to time of false alarms occurring. The probability that at least one false alarm will occur during some time interval  $t$  is:

Equation 2:

$$PFA = 1 - \exp(-FAR \times t).$$

As shown in Table 1, a 1.5 μs TOF is required for 220-meter range. Here, a 60 Hz FAR implies that, on average, one in every 11,363 range samples will be corrupted by a false positive. For the lidar sensor specified in Table 1, this is roughly 1,584 times per frame. Similarly, for a flash-lidar configuration, if there are  $N_{pixels}$  total pixels in an array, each characterized by the same FAR (in Hz), Poisson statistics can be applied to find the probability of at least one false alarm, anywhere within the array, during time interval  $t$ :

Equation 3:

$$P_{FA} = 1 - \exp(-FAR \times N_{pixels} \times t).$$

Using Equation 3, the probability of at least one false alarm is equal to one minus the probability of zero false alarms; the argument of the exponential function is equal to the

[7] P. F. McManamon, "Review of lidar: a historic, yet emerging, sensor technology with rich phenomenology," Optical Engineering (2012).

expected number of false alarms from the entire array over the period of observation.

Rice<sup>[8],[9]</sup> relates single-pixel FAR to the bandwidth (BW, in Hz) of the analog signal into the comparator, the detection threshold ( $n_{th}$ , in electrons), and the magnitude of the noise on the signal into the comparator ( $n_{noise}$ , in electrons) as:

Equation 4:

$$FAR = \sqrt{\frac{1}{3}} BW \exp\left[-\frac{n_{th}^2}{2n_{noise}^2}\right].$$

Physically speaking, both the detection threshold and the noisy signal into the pixel comparator are voltage quantities; for convenience of signal-level comparison, both quantities have been referred to the input node of the amplifier chain and expressed in units of electrons.

To find the condition that restricts  $n_{th}$ , Equation 3 and Equation 4 can be combined as follows:

Equation 5:

$$n_{th} = \sqrt{-2n_{noise}^2 \ln\left[-\frac{\sqrt{3} \ln(1 - P_{FA})}{N_{pixels} \times BW \times t}\right]}.$$

The approximations generally hold true for photodiodes, avalanche photodiodes (APDs) that operate at low gain or with ionization rate ratios close to  $k = 0$ , or when the primary electron count going into the avalanche gain process is large. In these cases, both the detector and amplifier noise processes can be approximated by normal distributions of pulse amplitude, and the PFA is a rapidly decreasing function of the ratio  $V_{th}/\sigma_{v,n}$  or, equivalently,  $n_{th}/n_{noise}$ , between the detection threshold and the standard deviation of the photoreceiver dark level.

However, the treatment of Equation 5 is not adequate for low-dark-current APDs operating at high avalanche gain with non-zero ionization rate ratio. All APDs generate excess noise due to the statistical nature of the avalanche process. The excess-noise factor,  $F$ , is the ratio of the mean square gain to the square of the mean gain; it is also the ratio by

which the spectral intensity of shot noise on the current of an APD exceeds that which would be expected from a noiseless multiplier on the basis of Poisson statistics alone.

The excess-noise factor is a function of both the gain,  $M$ , and the effective ionization coefficient ratio,  $k$ , of the APD. The first-order statistics of the excess-noise factor are normally calculated using a formula derived by McIntyre,<sup>[10]</sup> which is based on the assumption of an avalanche medium with uniform characteristics and an impact-ionization process that is independent of carrier history, expressed as:

Equation 6:

$$F(M, K) = M\left[1 - (1 - k)\left(\frac{M-1}{M}\right)^2\right].$$

The excess shot noise of an APD at a given gain depends on its effective ionization coefficient ratio, according to Equation 6. The values of the effective ionization coefficient ratio are significant because they correspond to different APD device technologies that are compatible with near-infrared-sensitive InGaAs absorbers. The most common InGaAs APDs have bulk InP multipliers characterized by  $k = 0.4$ . InGaAs APDs with thin InAlAs multipliers are characterized by  $k < 0.2$ , and Allegro has developed InGaAs APDs with multiple gain stages that can operate with  $k \sim 0.02$ .<sup>[11]</sup>

Most InGaAs APDs generate the majority of their primary dark current in their absorber, alongside the primary photocurrent generated by the optical signal and the background signals. In that case, dark carriers from primary dark current can be grouped with the background, as follows:

Equation 7:

$$n_{Qdark}^2 = n_{amp}^2 + \left(\langle a_{dark} \rangle + \langle a_{background} \rangle\right) M^2 F(M),$$

where  $n_{amp}^2$  is the noise from the amplifier,  $\langle a_{dark} \rangle$  is the mean of the primary dark-current charge deposited during the effective integration time, and  $\langle a_{background} \rangle$  is the primary background signal level within the effective integration time.

[8] S. O. Rice, "Mathematical Analysis of Random Noise," Bell System Technical Journal 23(3), pp. 282 – 332 (1944) doi: 10.1002/j.1538-7305.1944.tb00874.x

[9] S. O. Rice, "Mathematical Analysis of Random Noise," Bell System Technical Journal, 24(1), pp. 46-156 (1945), doi: 10.1002/j.1538-7305.1945.tb00453.x.

[10] R. J. McIntyre, "Multiplication Noise in Uniform Avalanche Diodes," IEEE Trans. Electron. Dev., 13(1), 164–168 (1966).

[11] G. M. Williams, D. A. Ramirez, M. M. Hayat, and A. S. Huntington, "Time resolved gain and excess noise properties of InGaAs/InAlAs avalanche photodiodes with cascaded discrete gain layer multiplication regions." J. Appl. Phys. 113(9), 093705 (2013). doi: 10.1063/1.4794345

It is often overlooked that, for APD photoreceivers, normal statistical methods cannot be used to calculate the PFA. After avalanche multiplication, each primary carrier injected into the multiplier of an APD may yield a different number of secondary carriers. For most linear-mode APDs, the statistical distribution of  $n$  output carriers resulting from an input of  $a$  primary carriers is that derived by McIntyre<sup>[12]</sup>:

Equation 8:

$$P_{McIntyre}(n) = \frac{a \Gamma\left[\frac{n}{1-k} + 1\right]}{n(n-a)! \times \Gamma\left[\frac{nk}{1-k} + 1 + a\right]} \times \left[\frac{1+k(M-1)}{M}\right]^{a+\frac{nk}{1-k}} \times \left[\frac{(1-k)(M-1)}{M}\right]^{n-a}$$

where  $k$  is the ratio of hole-to-electron impact-ionization rates,  $M$  is the average gain, and  $\Gamma$  is the Euler gamma function.

The McIntyre distribution has a pronounced positive skew. The importance of the value of  $k$  to the shape of the distribution and the resulting lidar receiver sensitivity is shown in Figure 3.

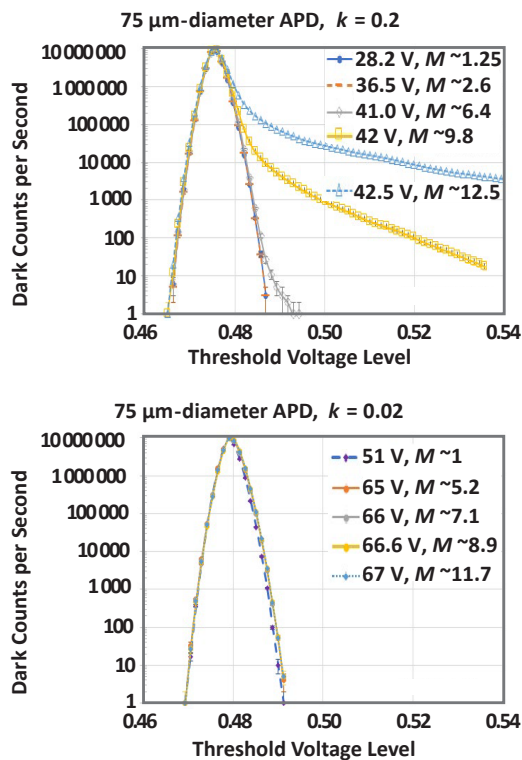


Figure 3: Dark-output distribution of photoreceivers for the cases of: a) a  $k = 0.2$  APD (top); and b) a  $k = 0.02$  APD (bottom), showing the tails of the distribution due to the McIntyre-distribution function cause a significant increase in false counts, even at modest gain—much more than the Gaussian assumption.

Figure 3 shows the false alarm rates measured on an APD photoreceiver for the cases of APDs with  $k = 0.2$  and  $k = 0.02$ , as a function of the threshold level. In Figure 3, a relative avalanche gain rather than an absolute avalanche gain is marked by the symbol  $M$ , because it was not possible to measure the gain operating point of the APD once it had been integrated into the receiver circuit. As shown in Figure 3, top, at a relative gain of approximately 6, the high-gain events from the distribution of the  $k = 0.2$  APD start to dominate the FAR, limiting the threshold values for this particular receiver to greater than 0.53 V for operation at 30 Hz FAR. However, in the case of the  $k = 0.02$  APD (Figure 3, bottom), even at relative gains of  $M = 11$ , the dark noise distribution is close to normal, and—for this particular receiver—30 Hz FAR can be achieved closer to a threshold of 0.49 V. At this voltage threshold level, the photon equivalent threshold level ( $n_{th}$ ) can be calculated using the measured conversion gain of the receiver.

The curves of Figure 3 can be modeled by replacing the bivariate normal distribution employed by Rice<sup>[8],[9]</sup> with the convolution of the APD gain distribution in Equation 8, with a normal distribution representing the amplifier noise. Writing the value of this convolution at an output level equal to the detection threshold as  $P_{RX}(n_{th})$ , substitution of the convolution into Rice's derivation of the FAR gives:

Equation 9:

$$FAR_{McIntyre} = \sqrt{\frac{2\pi}{3}} BW \times n_{noise} \times P_{RX}(n_{th}) \quad [\text{Hz}].$$

Except when making calculations for photon-counting applications, rigorous computation of the convolution of a McIntyre distribution with a normal distribution is unnecessary in order to calculate laser-pulse detection probability, PDE. Instead, the detection threshold required to achieve a given FAR ( $n_{th}$ ) can be combined with the average primary electron count generated by signal reception ( $\langle a_{signal} \rangle$ ) to find PDE as the value of the complementary cumulative distribution function of a normal distribution evaluated at the detection threshold:

Equation 10:

$$P_{DE} = 0.5 - 0.5 \operatorname{erf} \left[ \frac{n_{th} - \langle a_{signal} \rangle (M)}{\sqrt{2(n_{Q, dark}^2 + \langle a_{signal} \rangle M^2 F)}} \right].$$

The equivalent photon signal level can be determined by converting  $\langle a_{signal} \rangle$  to the input of the APD absorber by dividing by the quantum efficiency of the APD.

[12] R. J. McIntyre, "The Distribution of Gains in Uniformly Multiplying Avalanche Photodiodes: Theory," IEEE Trans. Electron. Devices ED-19(6), pp. 703-713 (1972). doi: 10.1117/12.2229068

## Time Resolution

To capture the TOF, the detector elements must include circuitry to timestamp reception of the laser-pulse echoes. Achieving 5 cm range resolution requires timestamps with ~333 ps resolution. Timestamps can be generated using either: a time-to-analog converter (TAC), which records the timestamp by sampling a time-variable voltage ramp; or a time-to-digital converter (TDC), which—upon the return of the pulse—latches the digital value of a counter, often with a vernier scale, developed from gate-delay elements, used for the least significant bits. Jitter, walk, and drift are the three major factors limiting time resolution.

In the absence of noise and amplitude variations, the leading-edge discriminator would mark the arrival time of each analog pulse with precision and consistency. However, practical systems include a non-negligible level of electronic noise, and this noise causes an uncertainty—or jitter—when the analog pulse crosses the discriminator threshold. If  $\sigma_n$  is the voltage amplitude of the noise superimposed on the analog pulse, and  $dV/dt$  is the slope of the signal when its leading edge crosses the discriminator threshold, the contribution of the noise to the timing jitter is:

Equation 11:

$$\sigma_j = \sigma_n / (dV/dt).$$

As shown in Figure 4, from Equation 11, the relationship is immediately apparent between the signal amplitude, detector gain, and amplifier transimpedance gain on the timing accuracy. If the noise cannot be reduced, the minimum timing jitter is obtained by setting the discriminator threshold for the point of maximum slope on the analog pulse. Thus, the fastest possible rise time from the signal source is preserved, a clear benefit.

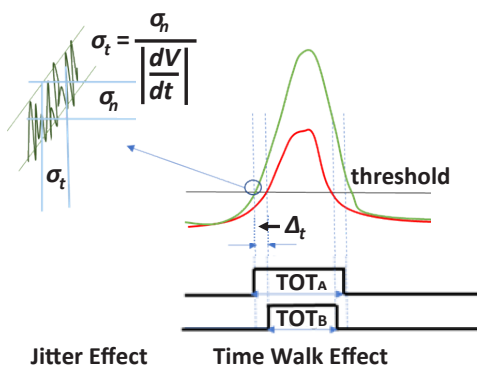


Figure 4: Illustration of the time-walk effect, including a time-over-threshold discriminator signal and a jitter effect.

Time walk is the systematic dependence of the timing on the amplitude of the input pulse. As shown in Figure 4, with a leading-edge timing discriminator, smaller pulses produce an output from the discriminator later than larger pulses, which leads to variable timing in response to the variations in the input-pulse amplitudes. Obviously, when a wide range of pulse amplitudes must be processed, time walk can seriously degrade the time resolution. To ensure precise timing, time walk must be minimized or eliminated. The recommended techniques to minimize time walk include amplitude-compensated measurements implemented using pulse-amplitude or time-over-threshold compensation, or through implementation of a constant-fraction-discrimination circuit.

## LIDAR SYSTEM DESIGN

### Infrared Transmitter

The available SWIR-transmitter sources include edge-emitting pulsed semiconductor laser diodes, erbium-doped fiber lasers, and erbium-doped glass diode-pumped solid-state (DPSS) lasers. The latter two choices best suited for long-range lidar. Fiber lasers allow the combination of short pulse durations with repetition rates up to ~1 million shots per second, at a practical upper pulse energy of ~1  $\mu$ J, whereas erbium-doped glass lasers can be configured for higher peak power, albeit generally with low repetition frequencies.

For example, consider the case of an Allegro test laser: a compact low-cost 1535 nm DPSS laser designed with 20  $\mu$ J pulse energy and 400 kHz pulse rate (shown in Figure 5) When the 20  $\mu$ J pulses are matched to 200 detector elements, each element receives approximately 100 nJ per pulse. This can achieve a range of 220 meters (see Figure 3) and can allow for 80 million angle-angle-range vectors to be obtained each second. This performance equates to approximately 1/9th of the full field of regard requirement specified in Table 1.



Figure 5: The Allegro test laser—a miniature 1535 nm DPSS laser, shown in comparison to the size of a quarter—has a beam quality of  $M^2 < 1.1 \times DL$  (diffraction limit) and can be operated at 20  $\mu$ J at up to a 400 kHz repetition rate. The laser was developed by the Allegro photonics group, then operating as Voxel.

## Lidar Photoreceivers

Because the photoreceiver sets the system sensitivity, its performance can affect average laser power significantly. Lidar photoreceivers typically include a photodetector, transimpedance amplifier (TIA), and pulse-detection circuit. At the 905 nm wavelength, the two primary solid-state photodetector options are silicon PIN photodiodes and silicon avalanche detectors. Both InGaAs and germanium detectors offer the potential for improved temporal response to 905 nm optical radiation compared to silicon. However, both detector types are more commonly operated at wavelengths beyond 1  $\mu$ m, where silicon does not respond. For 1.5  $\mu$ m operation, InGaAs photodiodes have higher bandwidth and less noise than germanium detectors.

To reduce the laser-pulse-energy requirements, APDs may be used. An APD is a special type of photodiode that amplifies photocurrent via an electron avalanche process. APDs can be operated in either linear mode or Geiger mode. In Geiger-mode operation, the APD is momentarily biased beyond its breakdown voltage, such that it may enter avalanche breakdown in response to signals as weak as a single photon. The penalty for the extreme sensitivity of Geiger mode is that Geiger-mode APDs cannot measure

the amplitude of multiphoton pulse returns, and they must be reset after they fire, before they re-arm. The dead time of a Geiger-mode APD can span a few nanoseconds for silicon to a few microseconds for InGaAs. In 3-D-imaging applications, the dead time prevents single-laser-shot reception of multiple target returns from objects closely spaced in range and makes Geiger-mode APDs susceptible to blinding by atmospheric backscattering or optical solar clutter. This hindrance limits the practical utility of Geiger-mode APDs for practical commercial lidar applications, especially for InGaAs Geiger-mode APDs.<sup>[13],[14]</sup>

In linear-mode operation, the average output of the APD is proportional to the strength of the optical signal, and the detector can operate continuously. Common SWIR-sensitive linear-mode APDs operate with average avalanche gain of approximately  $M < 50$ , more typically at  $M = 10$  to  $M = 20$ . Dark current is greater for the larger-diameter photodetectors typically used in scanned-lidar systems, and the excess-noise contribution to the shot noise limits the benefits of high avalanche gain.<sup>[15]</sup>

The FAR of an APD is often dominated by the excess noise of the dark-current contribution and the background-signal contributions. Furthermore, as introduced above, the distribution of the gain—not just its average value—has an impact on sensitivity.<sup>[16]</sup> Conventional InGaAs/InP APDs typically have bulk InP multiplication layers characterized by an ionization coefficient ratio of  $k \sim 0.4$ , which parameterizes the McIntyre excess-noise equation.<sup>[15]</sup> Allegro has developed a multi-stage APD, the single-carrier-multiplication (SCM) APD, which has gains that exceed 50 $\times$  with excess noise characterized by  $k \sim 0.02$ . The possibilities of improved sensitivity that can be achieved in such APDs by allowing for lower threshold settings with lower FAR is shown in Figure 3.

### Scanned Lidar Single-element InGaAs APD

**Photoreceivers:** When the FOV of the lidar photoreceiver is matched to the laser, background noise and susceptibility to multiple scattering factors are reduced, and long-range detection is achieved. For example, consider the test case of a test Allegro lidar photoreceiver that integrates an InGaAs APD detector, an amplification and pulse-processing application-specific integrated circuit (ASIC), and temperature-compensating biasing circuits, within

[13] G. M. Williams, Jr., "Limitations of Geiger-mode arrays for Flash LADAR applications," SPIE Proceedings 7684, Laser Radar Technology and Applications XV, 768414, May 04, 2010.

[14] P. F. McManamon, P. Banks, J. Beck, A. S. Huntington, and E. A. Watson, "A comparison flash lidar detector options," in SPIE Defense and Security, International Society for Optics and Photonics, May, pp. 983202-983202 (2016).

[15] R. J. McIntyre, "A new look at impact ionization-Part I: A theory of gain, noise, breakdown probability, and frequency response." IEEE Transactions on Electron Devices 46(8), pp. 1623-1631 (1999).

[16] G. M. Williams, et al., "Increased gain InGaAs avalanche photodiode with reduced excess noise achieved through asymmetric carrier modulation," J. Appl. Physics (2013).

a hermetic TO-8 package (shown in Figure 6). In this photoreceiver, the TIA bandwidth (tens of MHz) is much smaller than that of the photodiode (typically, a few GHz), and it defines the noise bandwidth. Examples of sensitivity measurements as a function of pulse width for an Allegro single-element InGaAs APD photoreceiver are shown in Figure 7; the noise-equivalent input (NEI) is ~50 – 100 photons, which is ~6 times lower than the 250-photon to 315-photon threshold sensitivity (60 Hz FAR).

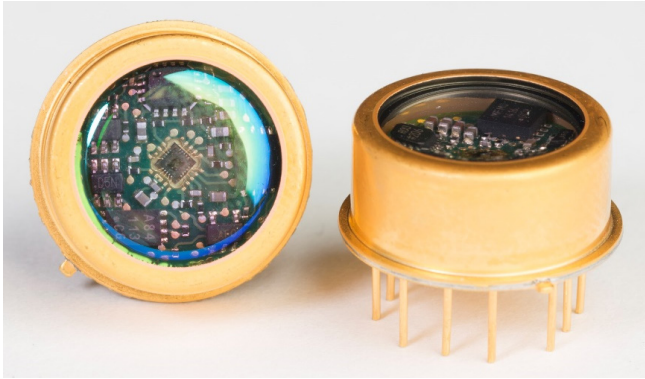


Figure 6: The Allegro APD lidar photoreceiver test device includes in-package temperature compensation and calibration.

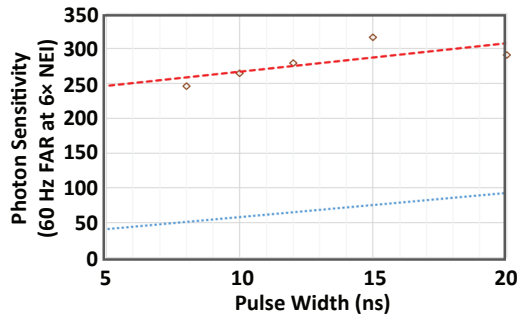


Figure 7: Measured sensitivity of an InGaAs APD photoreceiver is shown as a function of pulse width. Here, the higher conversion efficiency of the readout IC (ROIC) increases sensitivity for shorter pulse returns. The threshold sensitivity for 60 Hz FAR (red line; top) is ~6× the NEI (shown for reference; blue line; bottom).

### Staring Lidar and Step-Stare Lidar 2-D InGaAs

**Photoreceiver Sensor Arrays:** APDs of this type can also be made in sensor arrays. For example, consider the case of an Allegro test 128 x 128-element sensor array that captures the time and amplitude of three pulse returns in each pixel with 200 ps time resolution. This array achieves input-referred noise of 36 e<sup>-</sup>, made possible by the high conversion gain of the in-pixel amplifiers and the low-capacitance of the

linear-mode-APD InGaAs detector elements. The APDs have 80% quantum efficiency and, when operated at a gain of  $M = 20$ , allow for the possibility of an NEI level of less than three photons [ $36 / (80\% \times 20) = 2.25$  photons]. The plot of per-pixel NEI and sensitivity (for 30 Hz and 10 kHz FAR across the entire array) is shown in Figure 8, as a function of gain. As can be observed, due to the increased excess-shot noise of the dark current, there is an upper limit to useful APD gain. At higher operating gain, the positive skew of the pulse distribution of the avalanche gain process leads to an increase in excess noise. These effects can be mitigated through the use of a lower threshold setting and multipulse processing to enhance receiver sensitivity.

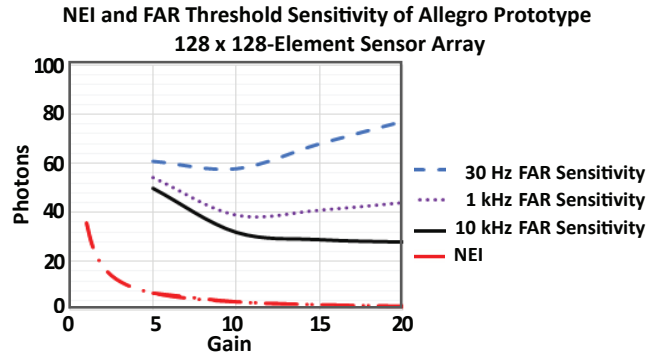


Figure 8: NEI as a function of gain for various laser-pulse widths for Allegro test sensor array.

### Mechanical and Non-Mechanical Scanners

Rotating-mirror systems are high-performance and, to date, have provided the primary testbed and development platform for the use of lidar in automated vehicles. To transition to low-cost compact lidar systems that can fit within the body panels of vehicles, developers must consider a number of alternatives.

Traditional laser-beam-steering systems (or scanners) are bulky, power-hungry, and vibration-prone mechanical systems. New small, lightweight, low-power devices are needed to steer the electro-optical laser beam. The ability to incorporate high mechanical stability and minimal hardware to steer a laser beam from its source to its target quickly, efficiently, and precisely will allow laser scanning—both in transmit and receive modes—to be used almost anywhere.

Alternative solutions to mechanical beam steering that have been explored include microlens arrays, micro-electro-mechanical systems,<sup>[17],[18]</sup> liquid-crystal polarization

[17] Thilo Sandner, et al., "Hybrid assembled micro scanner array with large aperture and their system integration for a 3-D ToF laser camera." SPIE OPTO. International Society for Optics and Photonics (2015).

[18] M. Helmer et al., "Challenges for MEMS based Scanning Laser System," 11th International Symposium on Automotive Lighting-ISAL 2015-Proceedings of the Conference 16, Herbert Utz Verlag (2015).

gratings,<sup>[19]</sup> holographic glasses, and birefringent prisms. All of these approaches suffer from low throughput, scattering, small steering angle/aperture, high fabrication cost, and/or large size/weight.

## Calibration and Clutter Rejection

To enable processors to perform the split-second decision making required for assisted-driver and self-driving cars, the sensor package must provide accurate 3-D data. This requires compensation for optical distortions, scanner pointing errors, mounting alignment, detector nonuniformity, nonlinearity due to signal amplitude as a function of range, target reflectance, target angle, and geo-referencing errors.

## CONCLUSION

In this work, key lidar sensor parameters—including operating wavelength, pulse energy, pulse frequency, receiver format, and receiver sensitivity—have been discussed in terms of the optimization of a design for a 360-degree eye-safe lidar system capable of 220-meter

range performance. Due to the higher MPE, along with less scattering and reduced solar clutter, the 1.5  $\mu\text{m}$  spectral range allows commercially available InGaAs APD detector technologies and erbium-doped DPSS lasers to be used in compact cost-effective sensor configurations. Due to the efficiencies gained by using higher-pulse-energy eye-safe lasers, the cost of this lidar technology scales more readily than lidar technologies that employ 905 nm emitters and detectors. A variety of scanning solutions are currently being evaluated to provide biaxial or coaxial sensor configurations.

---

[19] Scott R. Davis et al., "A lightweight, rugged, solid state laser radar system enabled by non-mechanical electro-optic beam steerers," SPIE Defense+ Security. International Society for Optics and Photonics (2016).

### Revision History

Number	Date	Description	Responsibility
–	March 9, 2022	Initial release	A. Huntington
1	March 17, 2022	Administrative corrections	A. Huntington
2	March 24, 2022	Minor terminology change: Autonomous changed to automated	A. Huntington

This document is based on the following published work:

© The Authors. Published by SPIE under a Creative Commons Attribution 3.0 Unported License. Distribution or reproduction of this work in whole or in part requires full attribution of the original publication, including its DOI.

George M. Williams “Optimization of eyesafe avalanche photodiode lidar for automobile safety and autonomous navigation systems,” *Optical Engineering* 56(3), 031224 (28 March 2017). <https://doi.org/10.1117/1.OE.56.3.031224>

Received: 4 August 2016; Accepted: 1 February 2017; Published: 28 March 2017

Copyright 2023, Allegro MicroSystems.

The information contained in this document does not constitute any representation, warranty, assurance, guaranty, or inducement by Allegro to the customer with respect to the subject matter of this document. The information being provided does not guarantee that a process based on this information will be reliable, or that Allegro has explored all of the possible failure modes. It is the customer’s responsibility to do sufficient qualification testing of the final product to ensure that it is reliable and meets all design requirements.

Copies of this document are considered uncontrolled documents.

MCO-0001197, Rev. 2  
P0180

955 PERIMETER ROAD • MANCHESTER, NH 03103 • USA  
+1-603-626-2300 • FAX: +1-603-641-5336 • ALLEGROMICRO.COM

